Melanin pigments extracted from horsehair as antibacterial agents

Tahmineh Rahmani Eliato^a, Joshua T. Smith^b, Zhen Tian^a, Eun-Sik Kim^c, Wonseok Hwang^d, Cheryl P. Andam^{be}, and Young Jo Kim^{*a}

Abstract

Here we present the important findings related to biologically derived pigments for potential use as antibacterial agents. Melanin biopigments extracted from *Equus ferus* hair exhibit homogeneous elliptical microstructure with highly ordered semicrystalline feature. Spectroscopic analysis indicates that melanin contains a high degree of redox active catechol groups, which can produce reactive oxygen species. The antibacterial activity of melanins was tested by incubating *Escherichia coli* and *Staphylococcus aureus* with melanins. Results showed 100% bacterial growth inhibition within 4 h. This finding suggests that melanin pigments may serve as naturally occurring antibacterial agents with unique redox chemistry and reactive oxygen species generation capability.

^a Department of Chemical Engineering, University of New Hampshire, Durham, NH 03824, USA.

^b Department of Molecular, Cellular and Biomedical Sciences, University of New Hampshire, Durham, NH 03824, USA.

^c Department of Environmental System Engineering, Chonnam National University, Yeosu, 59626, Republic of Korea.

^d Department of Chemistry and Biochemistry, University of Maryland, College Park, MD 20740, USA.

^e Department of Biological Sciences, University at Albany, State University of New York, Albany, NY 12222, USA.

^{*} To whom correspondence should be addressed: Fax: 1-603-862-3747; Tel: 1-603-862-2298 E-mail: youngjo.kim@unh.edu

Bacterial adherence and subsequent proliferation on solid surfaces are ongoing challenges in a variety of areas including daily consumables, industrial processes, and biomedical devices. The most common cause of biomedical implant failure is bacterial infection, which is exacerbated due to biofilm formation. Between 7-8 % of hernia repair surgical procedures result in infection and bacteria formation. Biofilm formation also leads to major challenges in wastewater treatment processes that use membranes. Membrane filtration is one of the most common approaches to convert effluents into water with acceptable level of impact to the environment by removing the ions and microorganisms. Such filtration techniques are affordable and cost-effective, however long-term use of a filter can promote biofilm formation which can consequently reduce its efficacy, and lifetime with increasing operational costs. Hence, development of effective strategies to minimize bacterial growth and prevent biofilm formation in these settings is critical.

Metal nanoparticles such as copper (Cu), titanium (Ti), silver (Ag), zinc (Zn), selenium (Se) and silicone (Si) have been studied for their antibacterial properties. ^{10–13} Oxidative stress generated by reactive oxygen species (ROS) and metal ion penetration into the bacteria are two main mechanisms that damage bacteria cells and lead to cell death. ^{14,15} However, there are many potential challenges associated with the depletion of metal ions from this class of metallic nanomaterials. Surface coating with polymers can be another approach to prevent biofouling and minimize bacterial growth on surfaces. Hydrophilic polymers such as polyethylene glycol and polyglycerol, or zwitterionic polymers such as 2-methacryloyloxyethyl phosphorylcholine and poly(sulfobetaine methacrylate) have been widely used to form a hydration layer on the surface to prevent bacterial adhesion and biofouling. ^{16–19} This hydration layer near the surface acts as a physical barrier and prevents direct contact between biomolecules and the surface. However, disordered disruption of polymeric surfaces in the complex media can result in potential challenges

that shortens the longevity.²⁰ Moreover, the disruption of biofilms using antibacterial agents requires concentrations that are 10-1000X higher than those that target isolated bacterial colonies.^{21,22} Both surface properties and surface area are two major factors that dictate biofilm formation.²³ The antibacterial agents that are biologically-derived, bioinert, scalable, and costeffective are therefore intrinsically advantageous.

As a subset of melanins, eumelanins (hereafter called melanins) are a broad class of biopigments that can be found in the skin, hair, iris of the eye, and neurosensorial tissues. $^{24-26}$ Melanins are largely composed of two subunits of 5,6-dihydroxyindole (DHI) and 5,6-dihydroxyindole-2-carboxylic acid (DHICA). These subunits are randomly stacked into planar macromolecular structures via π - π interactions to form homogeneous microstructures. Biological functions of melanins vary depending on their location in the physiological system however, the major role of melanins is to protect cells from radiation damage. Melanins contain diverse chemical functional groups such as redox-active catechols, pendant carboxylic acids, and aromatic amines, which allow conjugate bonding with a variety of cations including protons or metallic cations. Utility of these chemical features have allowed melanins to be used in many applications such as surgical meshes, biomedical imaging, cancer treating materials, functional coatings for tissue engineering, and aqueous charge storage devices. And a provide the storage devices are provided to the storage devices are provided to the storage devices.

Furthermore, recent studies have shown that catechol-embedded thin film composites can produce ROS by electrochemical insertion of ions and inhibit bacterial growth.^{37–39} Antimicrobial activities based on catechol chemistry have been reported from dopamine methacrylamide as well as melanins that are naturally sourced from fungi or bacteria.^{40–43} The unique structure of naturally-occurring melanins and the redox activity via catechol functional groups suggest that they can serve as biocompatible antibacterial agents. Herein we report the extraction of melanin

pigments from *Equus ferus* (horse) hair and investigate their antibacterial activity. Structures in micro- and meso-scale are examined by electron microscope and x-ray scattering techniques and the chemical functionalities are evaluated by spectroscopic tools. These structural and chemical analysis will assist to understand the structure-chemistry-property relationship of the naturally-occurring biopigment as an antibacterial agent.

Melanins from the hair are synthesized by specialized dendritic cells, which are melanocytes derived from the neural crest.⁴⁴ Various techniques have been applied to extract melanins from hair, i.e. base dissolution & acid isolation, dissolution in ionic liquid, and acid hydrolysis. Among these techniques, acid hydrolysis was used in this study due to facile extraction steps, which results in high purity and yield.⁴⁵ The initial E. ferus hair and resulting melanin powder (*Equus*Mel) after the acid hydrolysis extraction are shown in supporting Fig. S1 (a and b). The UV-vis absorption spectrum of EquusMel shows a monotonic decrease with no noticeable peak throughout the visible wavelength region, which is similar to other naturally-sourced melanin pigments (Fig. S1(c)). 46 The microstructure of Equus Mel is shown in Fig. 1 (a). Broadly, it shows an elliptical shape in the range of 638 ± 93.7 nm in length and 266.3 ± 56 nm in width. Compared to the homogeneous and spherical nanoparticle form factors of the naturally occurring melanins extracted from Sepia officinalis ink sac, EquusMel exhibits less homogeneous structure. 47 TEM images display the sub-nanometer scale textured microstructures, especially at the exterior of the individual particulates (Fig. 1(b and c)). Furthermore, both wide-angle (WAXS) and small-angle (SAXS) X-ray scattering measurements demonstrate that there is a noticeable scattering peak at q = 0.14 Å⁻¹. This is indicative of an ordered structure in *Equus*Mel with d-spacing of 45.2 Å (Fig. 1(d), Fig. S2(b)). Relatively weak and broad behavior was found from the higher order peaks at q $> 0.2 \text{ Å}^{-1}$, and the ratio of the scattering peaks did not match with other well-known structures such

as lamellae, or hexagonally packed cylinders. This ordered structure in meso-scale is considered as the spacing between the layers or the aperture of the fibril structure that is originated from the melanogenesis. 48,49 Melanogenesis is the biological process that takes place in specialized organelles called melanosomes. Melanosomes use enzymes, such as Pmel17, that catalyze polymerization reactions to control melanin assembly. Pmel17 assembles melanin protomolecules into large fibrils within melanosomes in vivo. 49,50 This natural synthesis mechanism leads to the extended fibrils and porous structure of EquusMel in meso-scale. Similar ordered arrangement can be found from the atomic force microscopy of the melanins isolated from S. officinalis ink, which reveals the presence of palisade-like filaments in the order of 3-6 nm.⁵¹ The semi-crystalline structure in meso-scale is largely a unique characteristic of various naturally-derived melanin pigments.⁵² Layered structure in sub-nanometer scale can be found from yak and human hair melanins and the melanins from S. officinalis ink sac, which exhibit ordered arrangement ranges from 2 to 6 Å. 52,53 Both microscopy and X-ray scattering data suggest that EquusMel largely consists of a fibril mesostructure with a distance of 45.2 Å. This unique structural feature of EquusMel is dissimilar with the synthetic melanins (SynMel) prepared by autooxidation of tyrosine, which contain amorphous topography. 35 The ordered meso-scale structure of Equus Mel can also be observed by measuring nitrogen physisorption. Pore size distribution of EquusMel determined by the Barret-Joyner-Halenda (BJH) method exhibits the presence of the primary pores within the range of 30-50 Å, which is in a good agreement with the d-spacing of 45.2 Å from WAXS and SAXS (Fig. 1(e)). In addition, N₂ adsorption-desorption isotherms indicate that Equus Mel contains Brunaur-Emmett-Teller (BET) surface area of 3 m²/g (Fig. 1(f)).⁵⁴ This BET surface area is slightly lower compared to those from the natural melanin from Sepia officinalis ink sac (19.9 m²/g), and the synthetic melanin (10.7 m²/g).³⁵ Equus Mel exhibits a type IV behavior

according to the presence of a rounded point at low values of p/p_o and an indistinct slope at intermediate values of p/p_o . These features correspond to the formation of monolayers and multilayers, respectively.

Chemical cues of *Equus*Mel and SynMel were interrogated by Fourier transform infrared spectroscopy (FTIR), confocal Raman spectroscopy, and X-ray photoelectron spectroscopy (XPS) (Fig. 2). FTIR spectra of both melanins exhibit no significant differences indicating similar chemical functionality. The broad band recorded at 3800-2800 cm⁻¹ is assigned to O-H stretching from carboxylic acid or catechol groups.⁵⁵ The peak centered at 1260 cm⁻¹ represents C-N stretching of pyrrole ring or O-H deformation of catechols.^{56,57} The peaks centered at 1650 and 1720 cm⁻¹ are attributed to conjugated C=C and vibration of aromatic C=O, which are present in both *Equus*Mel and SynMel.⁴⁷ Two distinct peaks at 2950-2850 cm⁻¹ were observed from *Equus*Mel but not from SynMel. These peaks are attributed to the stretching vibration of aliphatic C–H bonds that are induced by lipid or amino acid residues during extraction.⁵⁸⁻⁶⁰ Detailed FTIR peak assignments are summarized in Table S1.

Raman spectra of *Equus*Mel and SynMel exhibit the broad peak ranges between wavenumbers of 1000 and 2000 cm⁻¹. (Fig. 2(b)) These behaviors are associated with the vibrational mode of indole groups.^{61,62} Raman spectra were deconvoluted into five peaks (α - ϵ) that are designated to the known functional groups in melanin subunits.³² No significant peak shift was found between *Equus*Mel and SynMel, indicating the similarity in chemical signatures between both melanins. Deconvolved peak assignments are summarized in Table S2.

XPS was used to further examine the chemical contrast between *Equus*Mel and SynMel (Fig. 2(c)). Atomic weight percentages based on XPS survey peak indicate that *Equus*Mel contains more carbon and less oxygen and nitrogen compared to SynMel (Fig. 2(d)). Considering the carbon

as the main backbone of indole and the oxygen in the functional groups, we could speculate that a lower population of redox-active groups is present in Equus Mel compared to SynMel. A similar trend can be observed from the high-resolution C1s peak analysis. Each C1s peak was deconvolved into two peaks with the binding energies at 284.8, and 287.2 eV that are associated with C-C/C=C, and C-N/C-O functionalities, respectively. Peak area comparison between two peaks indicates higher population of C-N/C-O from SynMel than EquusMel (Fig. 2(e)). High-resolution O1s peaks enable to further quantify the distinction in the amount of redox-active functional groups that exists between EquusMel and SynMel. Deconvolved O1s peaks exhibit two peaks centered at 532.39, and 533.82 eV from EquusMel and 532.39, and 531.12 eV from SynMel. The peaks at 533.82, and 531.12 eV are attributed to COOH and C-O functionalities. The deviation of these two peaks could result from the vibrational energy difference of carboxylates that were synthesized via a different route. The major peak at 532.39 eV is assigned to C-OH from the catechol functional group.³⁵ Higher presence of C-OH group was found in EquusMel (90.51 %) compared to SynMel (81.03 %). Moreover, the association of the high-resolution O1s peak at 532.39 eV and the atomic weight percentage from the survey peak can provide insightful understanding about the potential population of redox-active catechol groups. EquusMel contains 14.65 % oxygen (survey peak), of which 90.51 % is present in C-OH chemical form, indicating the total C-OH population is 13.3 %. Similar assessment results in 19.9 % (81.03 % x 24.55 %) of the C-OH composition present in SynMel. Taken together, XPS analysis indicates that the redox-active catechol group of *Equus*Mel is approximately 1.5 times less than that of SynMel. It should be noted that exposure to acid during the extraction process may damage the structure, which could result in reducing the chemical functionalities of Equus Mel. 63

To study the antibacterial activity of melanin across two distinct bacterial taxa, we chose wellknown type strains of the gram-positive Staphylococcus aureus and the gram-negative Escherichia coli. Both species are common members of the human microflora but are also known to cause serious infections.⁶⁴ The antibacterial activity of both *Equus*Mel and SynMel melanins against *E*. coli and S. aureus was quantitatively evaluated using a colony count method after incubating each bacterial species ($c = 5 \times 10^5$ CFU/ml, V = 100 µl; CFU-colony forming units) with various melanin concentrations. Survival rates are depicted in Fig. 3 (a) and (c) after 4 h incubation. Both melanins generally exhibit significant decline in the number of CFUs of E. coli and S. aureus in comparison to the negative controls. Complete bacterial inhibition (i.e., no CFUs were observed) was achieved when incubated in melanin concentrations of 20 mg/ml and higher. This is comparable with antibacterial activity of natural cationic polymers such as chitosan. Chitosan is a positively charged polysaccharide synthesized by deacetylation of chitin. ⁶⁵ Qian et al. achieved 35 % and 50 % reduction in E. coli and S. aureus growth, respectively after co-incubation with chitosan nanoparticles (12 µg/ml) for 24 h.66 SynMel appears to have a greater impact in inhibiting bacterial growth than EquusMel at concentrations of 2.5 and 5 mg/ml. The variation of antibacterial activities between EquusMel and SynMel is correlated with the different density of redox-active functional groups that are present in each melanin. Table S4 summarizes the bactericidal activity of EquusMel and SynMel against E. coli and S. aureus. In addition, the difference of antibacterial activities may be due to the dissimilar surface characteristics of melanins. Static water contact angle measurement suggests that SynMel has a superhydrophilic surface (contact angle = 0°), while the EquusMel surface is hydrophobic (contact angle = $104.7 \pm$ 2.2°) (Fig. S4). The hydrophobic surface characteristics are ubiquitous and can be found from the melanins that are naturally sourced.⁵⁷ The inherent hydrophobic nature of EquusMel would

possibly lead to the aggregation of particles, hindering the full interface with bacteria. This contrast of surface properties could potentially lead to the lower antibacterial activity of *Equus*Mel.

Antibacterial activity via melanins is further examined by the time-course reduction of *E. coli* and *S. aureus*. We determined the growth inhibition of each bacteria by counting colonies at timepoints between 0 and 24 h, as shown in Fig. 4. Both *E. coli* and *S. aureus* exhibit substantial reduction in the number of CFUs throughout the measurement period in comparison to the monotonic growth of the controls. However, the time to complete bacterial inhibition varies between *Equus*Mel and SynMel. The growth of both bacterial species was completely suppressed after 2 h of incubation in SynMel while *Equus*Mel exhibited a slower response until 4 h of incubation. The delayed response of *Equus*Mel is associated with the inherent characteristic of *Equus*Mel that contains a lower density of redox-active catechol groups than SynMel. These rates of bacteria growth inhibition by both melanins are comparable to the recent studies. A recent study shows that growth curves obtained from incubation of chitosan nanoparticles with *S. aureus* V329 decreases in CFUs starting after 2 h.⁶⁵ In addition, Sarwar *et al.* observed complete bacterial growth inhibition after incubating chitosan at different molecular weights with *E. coli* and *S. aureus* for 8 h.⁶⁷

Generation of ROS by *Equus*Mel and SynMel was quantitatively corroborated by the H₂O₂ generation using a colorimetric assay. Oxidative stress by ROS is one of the main mechanisms that can damage the structure and function of proteins and other cellular components and may lead to cell death. Superoxide radical (O₂*-), hydroxyl radical (HO*), hydroperoxyl radical (HO₂*), singlet oxygen (¹O₂), and hydrogen peroxide (H₂O₂) are representatives of ROS.¹³ Among the ROS candidates, H₂O₂ is chosen in this study since it provides a quantitative result with facile

measurement.⁶⁸ Four different concentrations of *Equus*Mel and SynMel were incubated for 4 h in ddH₂O under ambient light, and H₂O₂ concentrations were measured (Fig. 5(a)). The colorimetric assay displays the increment of H₂O₂ generation as the concentrations of melanins increase. The concentrations of 2.5 mg/ml *Equus*Mel and 150 mg/ml SynMel reacted to form the lowest (0.56 μ M) and highest (129.8 μ M) concentrations of H₂O₂, respectively. It should be mentioned that at low concentration of H₂O₂, *E. coli* and *S. aureus* cells die as a result of damage to DNA, whereas at higher concentrations of H₂O₂, the death of the microorganism is due to damage to other part(s) of the cell.^{69,70} The outer structures of the gram-positive *S. aureus* and the gram-negative *E. coli* may explain differences in response to ROS exposure between these two species. *S. aureus* has an external peptidoglycan cell wall that can be directly attacked by ROS while *E. coli* has an outer membrane that provides greater protection against damage.^{71,72} Furthermore, the amounts of H₂O₂ produced from SynMel are 1.5 ± 0.2 times higher than *Equus*Mel. This is in close agreement with our findings of the chemical signatures of redox-active groups in *Equus*Mel. Spectroscopic data indicates that SynMel contains 49.6 % more catechol groups than *Equus*Mel.

The pro-oxidant property of melanins has been also reported in other literatures.⁶⁸ Catechols present in melanins are reversibly oxidized into ortho(*o*)-quinones by two-electron two-proton removal process. During oxidation, oxygen will react with electrons to form hydroxyl or superoxide radicals as an intermediate. The superoxides can further bind to protons to reproduce H₂O₂.⁷³ A proposed mechanism is shown in Fig. 5(b). A previous electron paramagnetic resonance (EPR) study in melanin shows that production of semiquinone and subsequent ROS is light- and water-driven, supporting the proposed antibacterial mechanism.⁷⁴ Moreover, another EPR study on catechol-containing material demonstrates ROS generation within the hydrated solution.⁷⁵ Although the exact antibacterial mechanism of melanin is still unclear, we cautiously posit that the

melanins are able to generate ROS by reversible oxidation of catechols, which can inhibit bacterial growth. Furthermore, the semicrystalline structure of *Equus*Mel may adversely affect its ability to promote the ROS since the multi-layered structure provides a kinetically disadvantageous environment to interact between superoxides and electrons/protons. The effect of light on the antibacterial activity was studied by storing the melanins in a dark environment for 7 days before bacterial incubation, which also occurred in the dark. The bacterial growth with melanins in the dark was observed to be slightly higher than in ambient light; however, the levels of bacteria growths from both conditions were significantly lower compared to the control sample (Fig. S5). This suggests that ROS can be produced by the melanins in the absence of light. Subsequently, antibacterial activity in this condition can occur due to the generation of hydroxyl free radical during the oxidation reaction of melanins (Fig. 5(b)). This demonstrates that ROS from melanins can be derived by both light and water into a variety of forms including superoxides, hydroxyls, or hydrogen peroxides, which can work as an effective antibacterial agent.

Conclusion

EquusMel extracted from E. ferus hair is examined by microscopic and spectroscopic approach. Electron microscopy verified the elliptical microstructure of EquusMel in nanoscale and the layer-by-layer stacked structure on the exterior surface. Highly organized multilayered structure of EquusMel was corroborated by x-ray scattering measurement, which exhibits ordered spacing of 45.2 Å. Spectroscopic techniques suggest that EquusMel contains similar chemical signatures to melanins extracted from S. officinalis and SynMel. Among various chemical functionalities, catechols are considered to be the main functional group that allows the reversible oxidation and reduction within the hydrated condition. ROS generated via oxidation of catechols is considered

the main mechanism of antibacterial activity, reaching 100 % cell death within 4 h. However, the lower densities of catechol groups present in *Equus*Mel resulted in less amount of ROS promotion compared to SynMel.

The results herein indicate that *Equus*Mel exhibits potential for naturally-derived biopigments to be utilized as functional antibacterial agents for a variety of applications. Antibacterial performance and kinetics can be further improved by molecular level modification of the surface of melanins to extend the redox functionalities. ^{76–78} Exfoliation of the layered structure of *Equus*Mel can also assist to maximize the interface resulting in the enhanced generation of ROS. ⁷⁹ These classes of biologically-derived melanins can be further applied in a variety of research and engineering areas. Fabrication of a composite membrane with *Equus*Mel would be advantageous to prevent biofilm formation and therefore increase the lifespan of the filtration process. ⁸⁰ In addition, melanins can be utilized to prepare antibacterial surfaces in biomedical applications including neural interface, biomedical electronics, medical consumables, or clinical equipment. ^{81,82}

Experimental

Materials.

Hydrochloric acid (HCl, ACS reagent, 37 %), acetone, ethanol, Synthetic melanin (SynMel) in analytical grade were purchased from Sigma-Aldrich (St. Louis, MO USA). *E. ferus* hair was collected from the Equine Facilities at the University of New Hampshire (Durham, NH USA). AmplexTM Red hydrogen peroxide/peroxidase assay kit was obtained from Invitrogen (Waltham, MA USA).

Extraction of Melanin from E. ferus Hair.

Melanin pigments extracted from black E. ferus hair were prepared as previously described using acid hydrolysis. Initially, the hair was washed thoroughly by acetone and ethanol (1:2 vol %) three times. Approximately 4 g of washed hair was vigorously stirred in a solution of 1 % HCl (V = 80 ml) to remove the water-soluble components. They were then mixed with 32 % HCl (V = 160 ml) followed by heating to 100 °C for 3 h. The solution was centrifuged at 3500 rpm for 5 min, and the precipitates were washed with double-distilled water (ddH₂O) four times. After discarding the supernatant, the sediment was dried in a vacuum oven overnight. Extracted melanin was kept in a closed container in darkness at ambient conditions until further processing.

Spectroscopic and Microscopic Characterization of Melanins.

As-prepared *Equus*Mel powder was fixed on Al stubs with double-sided carbon adhesive tape followed by Pt sputter coating. Images were taken using a scanning electron microscope (SEM, Lyra3 GMU FIB, Tescan, Brno, Czechia).

Small and wide-angle X-ray scattering (SAXS/WAXS) were performed using the in situ SAXS/WAXS Xeuss System (Xenocs, Grenoble, France) with a CuK α X-ray source ($\lambda = 1.5418$ Å, GeniX3D Cu ULD, Xenocs, SA, France) at 23°C. The scattering data were collected on a Pilatus (DECTRIS, Switzerland) over 6 frames with a 10 minutes acquisition time for each frame. The sample to detector distance (SDD) for SAXS/WAXS was 2464 mm and 365 mm, respectively, after the calibration using silver behenate (AgBe). Melanin in ethanol solution was suspended and dispersed using ultrasonic bath and dried in vacuum oven followed by placing in two Mylar films for SAXS/WAXS performance. The data of two Mylar films in an empty cell were collected as background. Six frames (600 s frame⁻¹) were collected for each sample, then normalized by the number of frames and circular averaged to obtain an intensity-wave vector (q) after background subtraction. Scattering images were analyzed using Igor Pro software (ver. 6.37) with the Irena package to obtain circular averaged 1D plots of intensity vs. scattering wave vector a. 83 Transmission Electron Microscopy was performed to analyze the shape and structure of *Equus*Mel particles using JEOL JEM 2100 LaB6. The particles solution was dropped on a carbon coated TEM grid (Structure Probe, Inc., West Chester, PA). Once the surface of the carbon coated TEM

particles using JEOL JEM 2100 LaB6. The particles solution was dropped on a carbon coated TEM grid (Structure Probe, Inc., West Chester, PA). Once the surface of the carbon coated TEM grids dried, it was transferred to the TEM grid holder and examined without staining. The acceleration voltage was set to 200 kV. All images were collected via the CCD camera attached to the TEM.

Raman spectra were collected using an AFM-Raman microscope (NTEGRA Spectra, NT-MDT Spectrum Instruments, Moscow, Russia) with a 10x objective and 500 nm wavelength laser over a Raman shift range of 800–2500 cm⁻¹. Data from five separate scans using 1 mW of laser power and 10 s exposure time were averaged to minimize sample degradation while maximizing the

signal-to-noise ratio. Raman peak deconvolution was performed using automatic multiple peak fit methods and viogt function (Originlab, Northampton, MA., USA).

Fourier transform infrared spectroscopy (FTIR) Spectra of melanin samples were directly measured with attenuated total reflection (ATR) technic (Is10 FTIR, Thermo Nicolet, Thermo Fisher Scientific, USA). Spectra were recorded in wavenumber range of 400-4000 cm⁻¹, resolution of 4 cm⁻¹ and 30 sample scans.

UV-Vis spectra of *Equus*Mel (200 μg/ml in DMSO) was measured by a spectrophotometer (Nanodrop 2000c, Thermo Scientific, USA) from a wavenumber range of 250-850 cm⁻¹.

X-ray Photoelectron Spectroscopy was performed using the Kratos Axis Supra XPS. Survey and high-resolution spectra of 1s orbitals of carbon (C), oxygen (O), and nitrogen (N) were obtained using Al source. Elemental analysis was done by the peak areas and the relative sensitivity factors of the instrumentation to individual atomic species. High-resolution spectra were further analyzed by CasaXPS software.

Specific surface area and pore size distribution of EquusMel was examined by nitrogen physisorption measurements using NOVA 2200E BET (Quantachrome Instrument) at 77.3 K. EquusMel was degassed at 200 °C for 12 h before BET measurements.

Static water contact angle was measured by sessile drop method using optical tensiometer (Theta lite Tensiometer, Biolin Scientific, Gothenburg, Sweden). 10 μ l of ddH₂O droplet was applied on the melanin pellet (50 mg) that was hydraulic pressed with pressure, p=4 metric tons at room temperature. Water contact angle was automatically calculated according to five point-traced droplet shapes.

Antibacterial Activity.

The antibacterial activity of EquusMel and SynMel biopolymers was evaluated using gramnegative Escherichia coli (E. coli, ATCC®15597TM) and gram-positive Staphylococcus aureus (S. aureus, ATCC®25923TM) strains. Prior to each antibacterial test, E. coli and S. aureus were streaked from a frozen glycerol stock onto lysogeny broth (LB) agar and commercially prepared tryptic soy agar with 10% sheep red blood cells (TSA-B) agar, respectively. A single bacterial colony was collected from the E. coli and S. aureus plates and inoculated in 5 mL of LB and brain heart infusion (BHI) liquid media, respectively. The cultures were incubated for 16 h at 37°C in a platform shaker. Bacterial growth concentrations were determined by means of optical density (OD) (Spectrophotometer, Nanodrop 2000c, Thermo Scientific, USA) at a 600 nm wavelength. Different concentrations of melanins (2.5, 5, 20, and 150 mg/ml) were inoculated with 5×10^5 CFU/ml bacteria suspensions ($V = 100 \mu l$) in a 96-well plate. The plates were incubated at 37°C for 1, 2, 4, and 24 h. Aliquots of the samples were serially diluted and plated on agar media for overnight incubation at 37°C. Visible colonies were counted and compared with the negative controls, which grown without melanins. Each experiment was repeated three times. The bactericidal activity rate (R) of the Equus Mel and SynMel was calculated according to following equation:

$$R = \frac{N_C - N_S}{N_C} \times 100 \%$$

where N_C represents average concentration of bacteria in control and N_S represents average concentration of bacteria when treated with a specific concentration of melanin.

In order to validate the role of light source, melanins were stored in the light free environment for 7 days before incubation with bacteria.

Pro-oxidant Activity Assay.

The level of H₂O₂ production was used as the metric for reactive oxygen species (ROS) generation. Melanins at different concentrations (2.5, 5, 20, and 150 mg/ml) were incubated with ddH₂O for 4 h under ambient condition. Aliquots of the aqueous solutions were assayed for the generation of H₂O₂ using Amplex Red reagent (ThermoFisher Scientific, Waltham, MA USA).⁸⁴ In brief, the assay detects the excitation and emission at wavelengths of 571 and 585 nm. The amount of H₂O₂ can be detected by the degree of oxidation from 10-acetyl-3,7-dihydroxyphenoxazine (ADHP) to resorufin. Data were measured using a fluorescence plate reader (SpectraMax M2e/EA, Molecular Devices, San Jose, CA USA). Each experiment was repeated three times.

Acknowledgement

The authors thanks to Brenda Hess-McAskill of UNH Equine Facilities for collecting *E. ferus* hair fibers and Amy Michaud at the Department of Molecular, Cellular and Biomedical Sciences for providing type strains of *S. aureus* and *E. coli*. The authors acknowledge the financial support provided by the following organizations: National Science Foundation EPSCoR award (1757371), UNH Collaborative Research Excellence (CoRE) Initiative, and UNH College of Engineering and Physical Sciences (CEPS).

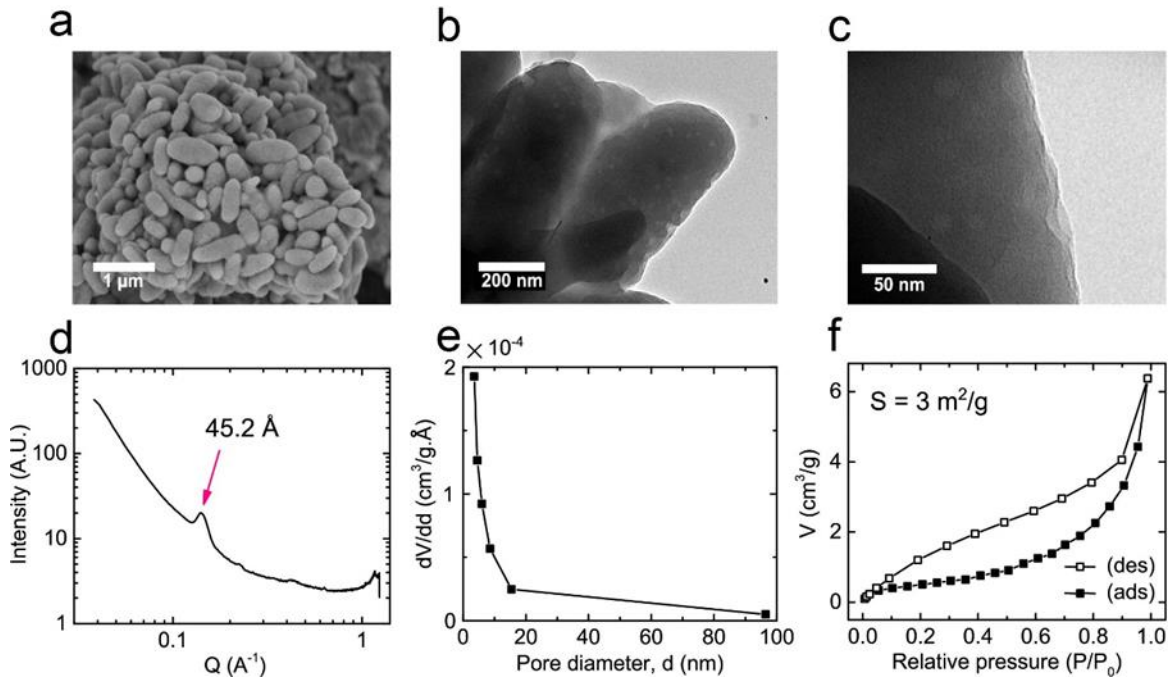


Fig. 1. (a) SEM and (b and c) TEM images of *Equus*Mel show the elliptical microstructure with mesoporous and layered structure within the individual particles. (d) Wide-angle X-ray scattering (WAXS) corroborates the presence of semicrystalline structure of *Equus*Mel in meso scale that largely contains the ordered layers with d-spacing of 45.2 Å. (e) Pore size distribution determined by Barrett-Joyner-Halenda method shows the existence of primary pores within the range of 30-50 Å. (f) Nitrogen adsorption-desorption isotherms exhibit the multilayered type IV structural behavior with BET surface area of 3 m²/g.

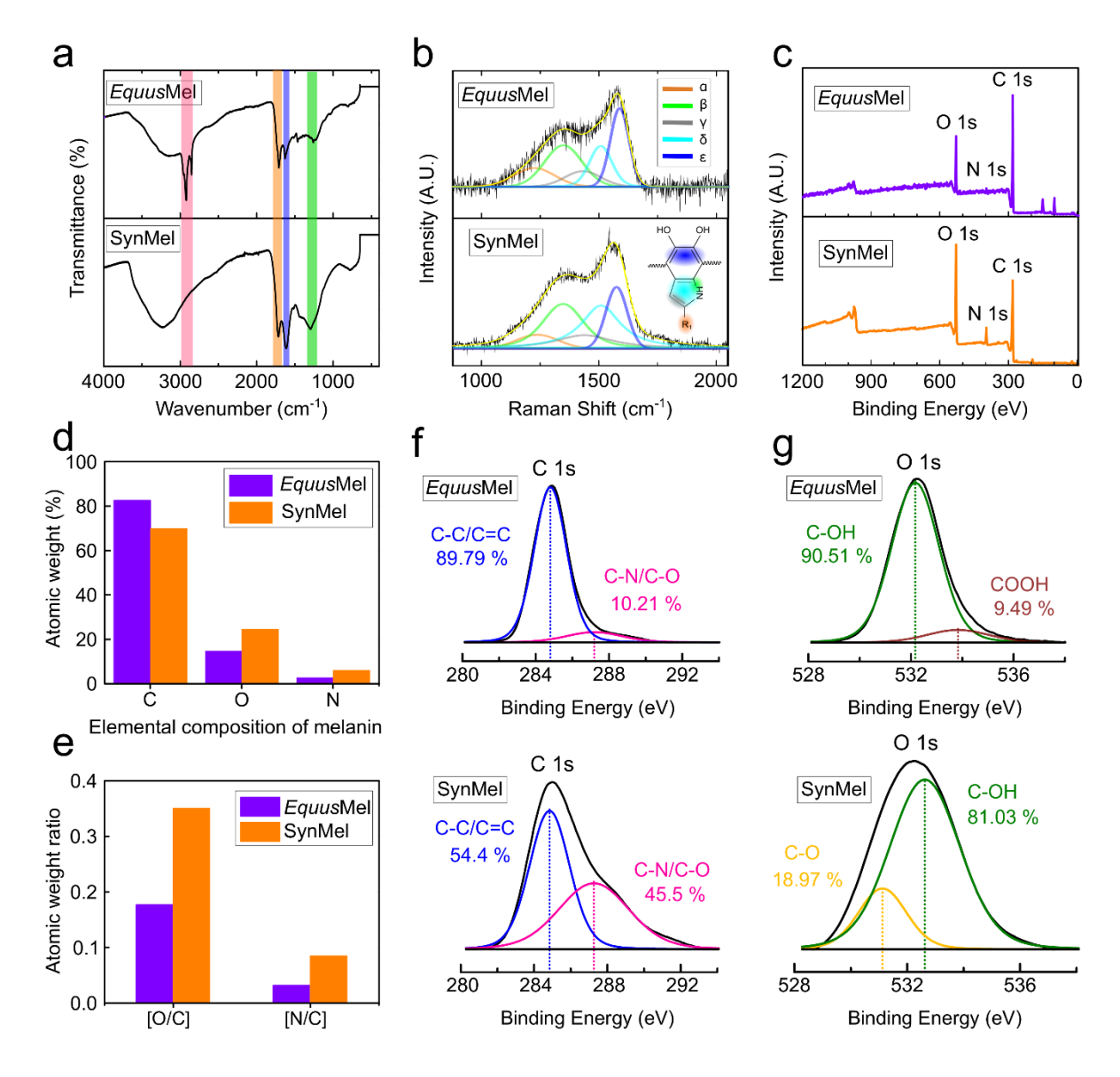


Fig. 2. (a) FTIR spectra of *Equus*Mel and SynMel. Two distinct peaks at 2850-2950 cm⁻¹ suggest the presence of the aliphatic C-H stretch in *Equus*Mel. (b) Raman spectra of *Equus*Mel and SynMel are deconvolved into five bands (α-ε). Black lines represent the raw spectra. Bindings are highlighted in the respective colors in the chemical structure of eumelanin. Functional group R₁ is COOH for SynMel and COOH or H for *Equus*Mel. (c) XPS are shown for *Equus*Mel and SynMel. The atomic weight percentages of melanins shown in (d) suggest that *Equus*Mel largely contains higher carbon and lower oxygen and nitrogen contents than SynMel. (e) Weight ratio of oxygen and nitrogen is shown based on the weight % of carbon. (f) High-resolution carbon peak indicates the higher presence of the aromatic C-C or C=C bonding compared to the C-N or C-O stretching. High-resolution peaks of oxygen in (g) corroborate the higher content of catechol groups from both *Equus*Mel and SynMel. High-resolution peaks are deconvolved by CasaXPS and shown as color lines. Detailed peak positions are summarized in supplementary Tables S1, S2, and S3.

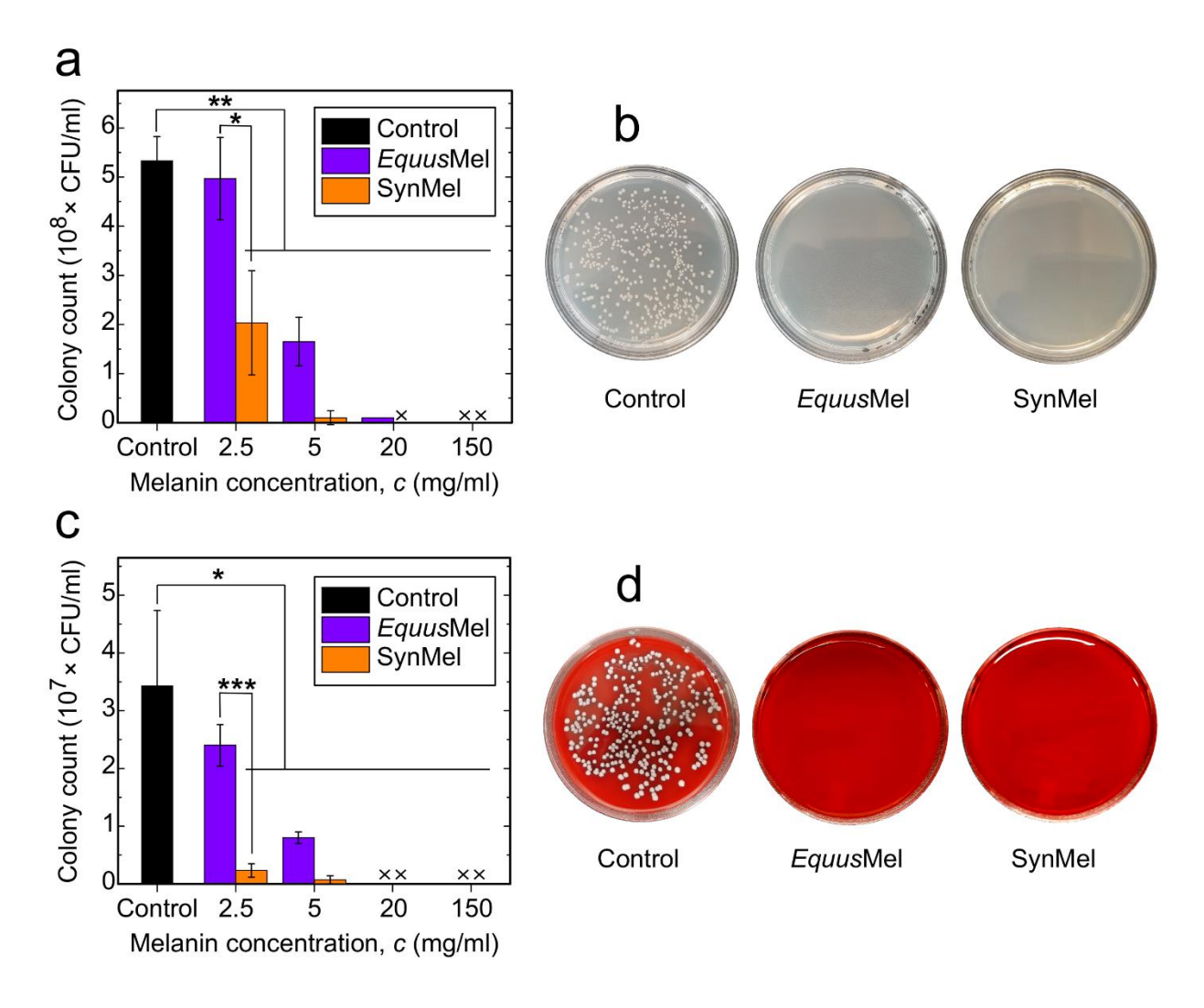


Fig. 3. *In vitro* antibacterial activities are tested using (a) *E. coli* and (c) *S. aureus*. Bacteria colony count was performed after 4 h exposure to *Equus*Mel and SynMel at 37 °C with four different concentrations. Bacterial growth is broadly suppressed compared to the controls. Apart from 2.5 mg/ml *Equus*Mel, all concentrations of both melanins exhibits significant decreases in bacterial growth for both *E. coli* and *S. aureus*. X indicates zero colonies. Data are presented as mean \pm SD (n = 3). Statistically significant differences are indicated by ***p < 0.001, **p < 0.01, and *p < 0.05 compared to the control. Detailed bactericidal activities are given in supplementary Table S4. Representative images of agar plates are shown after incubating (b) *E. coli* and (d) *S. aureus* in melanins (150 mg/ml) for 4 h at 37 °C.

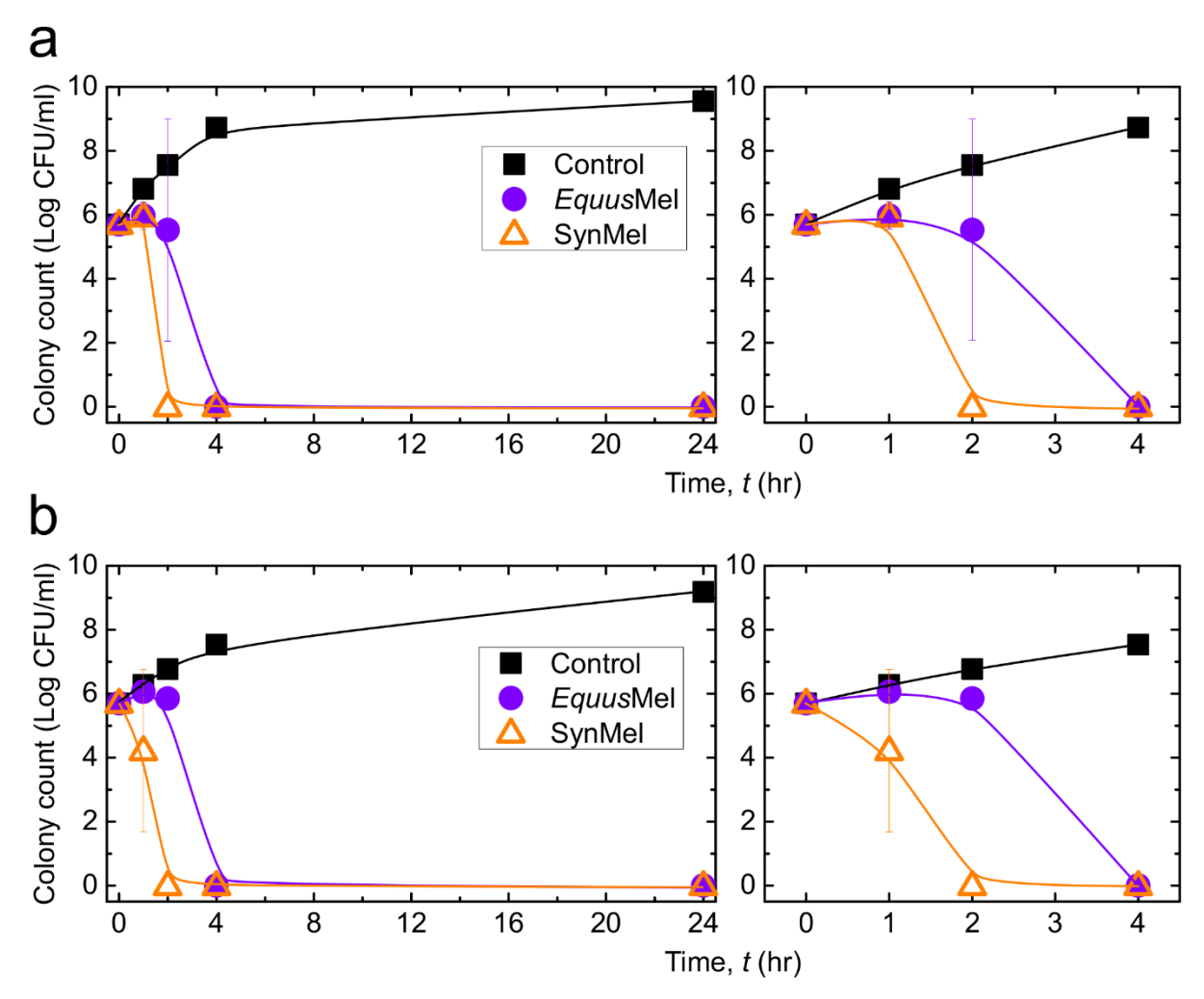


Fig. 4. Temporal kinetics of bacterial reduction is shown for (a) *E. coli*, and (b) *S. aureus* through 24 h incubation at 37 °C. *Equus*Mel exhibits a slight delayed response until 2 h compared to SynMel, however 100 % reduction is achieved for both melanins after 4 h of incubation. Bacteria incubation was performed at 37 °C with a melanin concentration of 150 mg/ml under ambient light (n = 3). Graphs on the right column show the enlarged view of the full measurements. Trendlines are generated by interpolating the measured data.

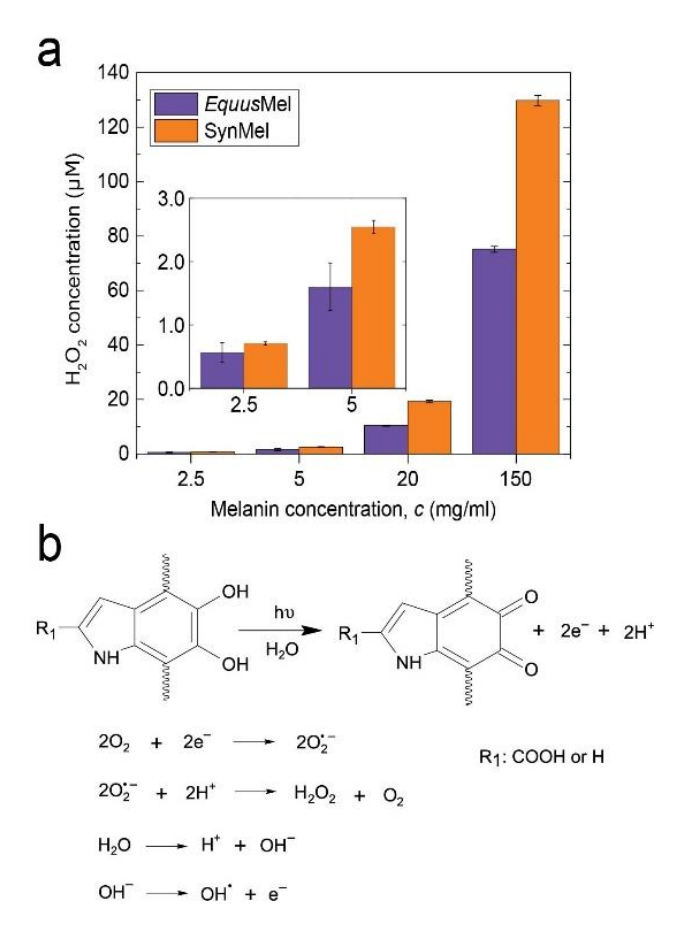


Fig. 5. (a) The measured concentrations of hydrogen peroxide generated by four defined concentrations of melanins. Measurements were performed by colorimetry assay in 4 h after the aqueous solution under ambient light (n = 3). Inset displays the magnified values from 2.5 and 5 mg/ml. (b) Proposed mechanism of ROS generation by melanins is shown. Photo-oxidation of melanins induces two electrons and protons leading to the production of superoxides. Superoxides and free protons can incorporate to reproduce H_2O_2 . Another possible form of ROS is the hydroxyl free radical that promotes the antibacterial activity in the absence of light. Antibacterial activity of melanins in the dark environment (7 days) can be found from the supporting information Fig. S5.

Reference

- S. Galié, C. García-Gutiérrez, E. M. Miguélez, C. J. Villar and F. Lombó, *Front. Microbiol.*, 2018, **9**, 898.
- Z. Khatoon, C. D. McTiernan, E. J. Suuronen, T.-F. Mah and E. I. Alarcon, *Heliyon*, 2018, 4, e01067.
- 3 J. S. VanEpps and J. G. Younger, *Shock*, 2016, **46**, 597–608.
- 4 C. R. Arciola, D. Campoccia and L. Montanaro, *Nat. Rev. Microbiol.*, 2018, **16**, 397–409.
- 5 A. Rios, J. Rodriguez, V. Munitiz, P. Alcaraz, P. D. Flores and P. Parrilla, *Hernia*, 2001, **5**, 148–152.
- M. D. Firouzjaei, S. F. Seyedpour, S. A. Aktij, M. Giagnorio, N. Bazrafshan, A. Mollahosseini, F. Samadi, S. Ahmadalipour, F. D. Firouzjaei, M. R. Esfahani, A. Tiraferri, M. Elliott, M. Sangermano, A. Abdelrasoul, J. R. McCutcheon, M. Sadrzadeh, A. R. Esfahani and A. Rahimpour, *J. Membr. Sci.*, 2020, 596, 117604.
- 7 Q. Shen, S.-J. Xu, Z.-Q. Dong, H.-Z. Zhang, Z.-L. Xu and C. Y. Tang, *J. Membr. Sci.*, 2020, **610**, 118220.
- 8 R. Li, Y. Wu, L. Shen, J. Chen and H. Lin, *J. Colloid Interface Sci.*, 2018, **531**, 493–501.
- 9 G. Zhang, J. Lv and F. Yang, *Water Sci. Technol.*, 2019, **79**, 1437–1446.
- N. S. Leyland, J. Podporska-Carroll, J. Browne, S. J. Hinder, B. Quilty and S. C. Pillai, *Sci. Rep.*, 2016, **6**, 24770.
- J. Podporska-Carroll, A. Myles, B. Quilty, D. E. McCormack, R. Fagan, S. J. Hinder, D.
 D. Dionysiou and S. C. Pillai, *J. Hazard. Mater.*, 2017, 324, 39–47.
- A. Nastulyavichus, S. Kudryashov, N. Smirnov, I. Saraeva, A. Rudenko, E. Tolordava, A. Ionin, Y. Romanova and D. Zayarny, *Appl. Surf. Sci.*, 2019, **469**, 220–225.
- A. Khezerlou, M. Alizadeh-Sani, M. Azizi-Lalabadi and A. Ehsani, *Microb. Pathog.*, 2018, **123**, 505–526.
- B. Ezraty, A. Gennaris, F. Barras and J.-F. Collet, *Nat. Rev. Microbiol.*, 2017, **15**, 385–396.
- 15 F. C. Fang, *mBio*, 2011, **2**, e00141-11.
- 16 A. B. Asha, Y. Chen, H. Zhang, S. Ghaemi, K. Ishihara, Y. Liu and R. Narain, *Langmuir*, 2019, **35**, 1621–1630.

- I. Francolini, I. Silvestro, V. Di Lisio, A. Martinelli and A. Piozzi, *Int. J. Mol. Sci.*, 2019, 20, 1001.
- 18 Q. Wei, T. Becherer, P.-L. M. Noeske, I. Grunwald and R. Haag, *Adv. Mater.*, 2014, **26**, 2688–2693.
- 19 S. Jiang and Z. Cao, *Adv. Mater.*, 2010, **22**, 920–932.
- 20 H. Qian, J. Yang, Y. Lou, O. ur Rahman, Z. Li, X. Ding, J. Gao, C. Du and D. Zhang, *Appl. Surf. Sci.*, 2019, **465**, 267–278.
- D. Sharma, L. Misba and A. U. Khan, Antimicrob. Resist. Infect. Control, 2019, 8, 76.
- L. Dieltjens, K. Appermans, M. Lissens, B. Lories, W. Kim, E. V. Van der Eycken, K. R. Foster and H. P. Steenackers, *Nat. Commun.*, 2020, **11**, 107.
- G. Feng, Y. Cheng, S.-Y. Wang, D. A. Borca-Tasciuc, R. W. Worobo and C. I. Moraru, *Npj Biofilms Microbiomes*, 2015, **1**, 15022.
- 24 A. A. R. Watt, J. P. Bothma and P. Meredith, *Soft Matter*, 2009, **5**, 3754.
- A. R. Katritzky, N. G. Akhmedov, S. N. Denisenko and O. V. Denisko, *Pigm. Cell Res.*, 2002, **15**, 93–97.
- F. A. Zucca, E. Basso, F. A. Cupaioli, E. Ferrari, D. Sulzer, L. Casella and L. Zecca, *Neurotox. Res.*, 2014, **25**, 13–23.
- 27 M. d'Ischia, A. Napolitano, A. Pezzella, P. Meredith and T. Sarna, *Angew. Chem. Int. Ed.*, 2009, **48**, 3914–3921.
- 28 F. Solano, Int. J. Mol. Sci., 2017, 18, 1561.
- L. Panzella, G. Gentile, G. D'Errico, N. F. Della Vecchia, M. E. Errico, A. Napolitano, C. Carfagna and M. d'Ischia, *Angew. Chem. Int. Ed.*, 2013, **52**, 12684–12687.
- 30 M. Brenner and V. J. Hearing, *Photochem. Photobiol.*, 2008, **84**, 539–549.
- 31 Y. J. Kim, W. Wu, S.-E. Chun, J. F. Whitacre and C. J. Bettinger, *Adv. Mater.*, 2014, **26**, 6572–6579.
- 32 Y. J. Kim, A. Khetan, W. Wu, S.-E. Chun, V. Viswanathan, J. F. Whitacre and C. J. Bettinger, *Adv. Mater.*, 2016, **28**, 3173–3180.
- T. Repenko, A. Rix, A. Nedilko, J. Rose, A. Hermann, R. Vinokur, S. Moli, R. Cao-Milàn, M. Mayer, G. von Plessen, A. Fery, L. De Laporte, W. Lederle, D. N. Chigrin and A. J. C. Kuehne, *Adv. Funct. Mater.*, 2018, **28**, 1705607.

- 34 H. Cheng, K. Yue, M. Kazemzadeh-Narbat, Y. Liu, A. Khalilpour, B. Li, Y. S. Zhang, N. Annabi and A. Khademhosseini, *ACS Appl. Mater. Interfaces*, 2017, **9**, 11428–11439.
- 35 Y. J. Kim, W. Wu, S.-E. Chun, J. F. Whitacre and C. J. Bettinger, *Proc. Natl. Acad. Sci.*, 2013, **110**, 20912–20917.
- 36 M. Caldas, A. C. Santos, F. Veiga, R. Rebelo, R. L. Reis and V. M. Correlo, *Acta Biomater.*, 2020, 105, 26–43.
- E. Kim, Y. Liu, C. J. Baker, R. Owens, S. Xiao, W. E. Bentley and G. F. Payne, *Biomacromolecules*, 2011, **12**, 880–888.
- E. Kim, Y. Liu, W. T. Leverage, J.-J. Yin, I. M. White, W. E. Bentley and G. F. Payne, *Biomacromolecules*, 2014, **15**, 1653–1662.
- 39 H. Liu, X. Qu, E. Kim, M. Lei, K. Dai, X. Tan, M. Xu, J. Li, Y. Liu, X. Shi, P. Li, G. F. Payne and C. Liu, *Biomaterials*, 2018, **162**, 109–122.
- 40 B. Liu, C. Zhou, Z. Zhang, J. D. Roland and B. P. Lee, *Chem. Eng. J.*, 2021, **403**, 126340.
- H. Meng, P. K. Forooshani, P. U. Joshi, J. Osborne, X. Mi, C. Meingast, R. Pinnaratip, J. Kelley, A. Narkar, W. He, M. C. Frost, C. L. Heldt and B. P. Lee, *Acta Biomater.*, 2019, 83, 109–118.
- 42 C. Xu, J. Li, L. Yang, F. Shi, L. Yang and M. Ye, Food Control, 2017, 73, 1445–1451.
- P. Manivasagan, J. Venkatesan, K. Senthilkumar, K. Sivakumar and S.-K. Kim, *Int. J. Biol. Macromol.*, 2013, **58**, 263–274.
- 44 L. Xiao, R. Zhang and W. Zhu, *Micron*, 2019, **119**, 109–116.
- 45 Y. Liang, Q. Han, N. Byrne, L. Sun and X. Wang, *Fibers Polym.*, 2018, **19**, 1640–1646.
- P. Meredith, B. J. Powell, J. Riesz, S. P. Nighswander-Rempel, M. R. Pederson and E. G. Moore, *Soft Matter*, 2006, **2**, 37–44.
- I.-E. Pralea, R.-C. Moldovan, A.-M. Petrache, M. Ilieş, S.-C. Hegheş, I. Ielciu, R. Nicoară, M. Moldovan, M. Ene, M. Radu, A. Uifălean and C.-A. Iuga, *Int. J. Mol. Sci.*, 2019, **20**, 3943.
- T. Imai, K. Higuchi, Y. Yamamoto, S. Arai, T. Nakano and N. Tanaka, *Microscopy*, 2016, **65**, 185–189.
- 49 I. Hurbain, W. J. C. Geerts, T. Boudier, S. Marco, A. J. Verkleij, M. S. Marks and G. Raposo, *Proc. Natl. Acad. Sci.*, 2008, **105**, 19726–19731.

- 50 A. K. Chakraborty, J. T. Platt, K. K. Kim, B. Kwon, D. C. Bennett and J. M. Pawelek, *Eur. J. Biochem.*, 1996, **236**, 180–188.
- 51 C. M. R. Clancy and J. D. Simon, *Biochemistry*, 2001, **40**, 13353–13360.
- 52 Z. Tian, W. Hwang and Y. J. Kim, *J. Mater. Chem. B*, 2019, **7**, 6355–6361.
- 53 W. Xie, F. Yan, E. Pakdel, J. Sharp, D. Liu, X. Wang, S. Zhan and L. Sun, *ACS Biomater. Sci. Eng.*, 2020, **6**, 5305–5314.
- M. Thommes, K. Kaneko, A. V. Neimark, J. P. Olivier, F. Rodriguez-Reinoso, J. Rouquerol and K. S. W. Sing, *Pure Appl. Chem.*, 2015, **87**, 1051–1069.
- Y. Liu, L. Hong, K. Wakamatsu, S. Ito, B. Adhyaru, C.-Y. Cheng, C. R. Bowers and J. D. Simon, *Photochem. Photobiol.*, 2005, **81**, 135.
- 56 L.-F. Wang and J.-W. Rhim, *LWT*, 2019, **99**, 17–23.
- 57 N. E.-A. El-Naggar and S. M. El-Ewasy, Sci. Rep., 2017, 7, 42129.
- 58 Q. Xing, P. Buono, D. Ruch, P. Dubois, L. Wu and W.-J. Wang, *ACS Sustain. Chem. Eng.*, 2019, 7, 4147–4157.
- 59 W. Xie, E. Pakdel, D. Liu, L. Sun and X. Wang, *ACS Sustain. Chem. Eng.*, 2020, **8**, 1343–1352.
- M. Lozano, P. Rodríguez-Ulibarri, J. C. Echeverría, M. Beruete, M. Sorolla and M. J. Beriain, *Food Anal. Methods*, 2017, **10**, 3462–3470.
- 61 S. A. Centeno and J. Shamir, *J. Mol. Struct.*, 2008, **873**, 149–159.
- V. Capozzi, G. Perna, A. Gallone, P. F. Biagi, P. Carmone, A. Fratello, G. Guida, P. Zanna and R. Cicero, *J. Mol. Struct.*, 2005, **744–747**, 717–721.
- 63 S. Ito, *Biochim. Biophys. Acta BBA Gen. Subj.*, 1986, **883**, 155–161.
- E. Tacconelli, E. Carrara, A. Savoldi, S. Harbarth, M. Mendelson, D. L. Monnet, C. Pulcini, G. Kahlmeter, J. Kluytmans, Y. Carmeli, M. Ouellette, K. Outterson, J. Patel, M. Cavaleri, E. M. Cox, C. R. Houchens, M. L. Grayson, P. Hansen, N. Singh, U. Theuretzbacher, N. Magrini, A. O. Aboderin, S. S. Al-Abri, N. Awang Jalil, N. Benzonana, S. Bhattacharya, A. J. Brink, F. R. Burkert, O. Cars, G. Cornaglia, O. J. Dyar, A. W. Friedrich, A. C. Gales, S. Gandra, C. G. Giske, D. A. Goff, H. Goossens, T. Gottlieb, M. Guzman Blanco, W. Hryniewicz, D. Kattula, T. Jinks, S. S. Kanj, L. Kerr, M.-P. Kieny, Y. S. Kim, R. S. Kozlov, J. Labarca, R. Laxminarayan, K. Leder, L. Leibovici, G. Levy-Hara, J. Littman, S. Malhotra-Kumar, V. Manchanda, L. Moja, B.

- Ndoye, A. Pan, D. L. Paterson, M. Paul, H. Qiu, P. Ramon-Pardo, J. Rodríguez-Baño, M. Sanguinetti, S. Sengupta, M. Sharland, M. Si-Mehand, L. L. Silver, W. Song, M. Steinbakk, J. Thomsen, G. E. Thwaites, J. W. van der Meer, N. Van Kinh, S. Vega, M. V. Villegas, A. Wechsler-Fördös, H. F. L. Wertheim, E. Wesangula, N. Woodford, F. O. Yilmaz and A. Zorzet, *Lancet Infect. Dis.*, 2018, **18**, 318–327.
- 65 M. S. Orellano, P. Isaac, M. L. Breser, L. P. Bohl, A. Conesa, R. D. Falcone and C. Porporatto, *Carbohydr. Polym.*, 2019, **213**, 1–9.
- 66 J. Qian, C. Pan and C. Liang, *Eng. Life Sci.*, 2017, **17**, 629–634.
- 67 A. Sarwar, H. Katas and N. M. Zin, *J. Nanoparticle Res.*, 2014, **16**, 2517.
- 68 H. Liu, X. Qu, H. Tan, J. Song, M. Lei, E. Kim, G. F. Payne and C. Liu, *Acta Biomater*., 2019, **88**, 181–196.
- 69 E. Linley, S. P. Denyer, G. McDonnell, C. Simons and J.-Y. Maillard, *J. Antimicrob*. *Chemother.*, 2012, **67**, 1589–1596.
- 70 J. A. Imlay and S. Linn, *J. Bacteriol.*, 1986, **166**, 519–527.
- M. Exner, S. Bhattacharya, B. Christiansen, J. Gebel, P. Goroncy-Bermes, P. Hartemann, P. Heeg, C. Ilschner, A. Kramer, E. Larson, W. Merkens, M. Mielke, P. Oltmanns, B. Ross, M. Rotter, R. M. Schmithausen, H.-G. Sonntag and M. Trautmann, *GMS Hyg. Infect. Control* 2017, 12, 2196-5226.
- 72 Z. Breijyeh, B. Jubeh and R. Karaman, *Molecules*, 2020, **25**, 1340.
- 73 M. Hayyan, M. A. Hashim and I. M. AlNashef, *Chem. Rev.*, 2016, **116**, 3029–3085.
- A. B. Mostert, S. B. Rienecker, C. Noble, G. R. Hanson and P. Meredith, *Sci. Adv.*, 2018, **4**, eaaq1293.
- 75 Z. Zhang, X. He, C. Zhou, M. Reaume, M. Wu, B. Liu and B. P. Lee, *ACS Appl. Mater. Interfaces*, 2020, **12**, 21210–21220.
- A. Lampel, S. A. McPhee, H.-A. Park, G. G. Scott, S. Humagain, D. R. Hekstra, B. Yoo,
 P. W. J. M. Frederix, T.-D. Li, R. R. Abzalimov, S. G. Greenbaum, T. Tuttle, C. Hu, C. J.
 Bettinger and R. V. Ulijn, *Science*, 2017, 356, 1064–1068.
- 77 W.-Z. Qiu, H.-C. Yang and Z.-K. Xu, *Adv. Colloid Interface Sci.*, 2018, **256**, 111–125.
- 78 K.-Y. Ju, Y. Lee, S. Lee, S. B. Park and J.-K. Lee, *Biomacromolecules*, 2011, **12**, 625–632.

- 79 D. Wei, L. Grande, V. Chundi, R. White, C. Bower, P. Andrew and T. Ryhänen, *Chem Commun*, 2012, **48**, 1239–1241.
- L. C. Capozzi, F. M. Mehmood, M. Giagnorio, A. Tiraferri, M. Cerruti and M. Sangermano, *Macromol. Mater. Eng.*, 2017, **302**, 1600481.
- 81 I. S. Kwon, Y. J. Kim, L. Klosterman, M. Forssell, G. K. Fedder and C. J. Bettinger, *J. Mater. Chem. B*, 2016, **4**, 3031–3036.
- J. Luo, A. S. Meyer, R. V. Mateiu, D. Kalyani and M. Pinelo, *ACS Appl. Mater. Interfaces*, 2014, **6**, 22894–22904.
- 83 J. Ilavsky and P. R. Jemian, *J. Appl. Crystallogr.*, 2009, **42**, 347–353.
- D. Dębski, R. Smulik, J. Zielonka, B. Michałowski, M. Jakubowska, K. Dębowska, J. Adamus, A. Marcinek, B. Kalyanaraman and A. Sikora, *Free Radic. Biol. Med.*, 2016, **95**, 323–332.

Supporting Information

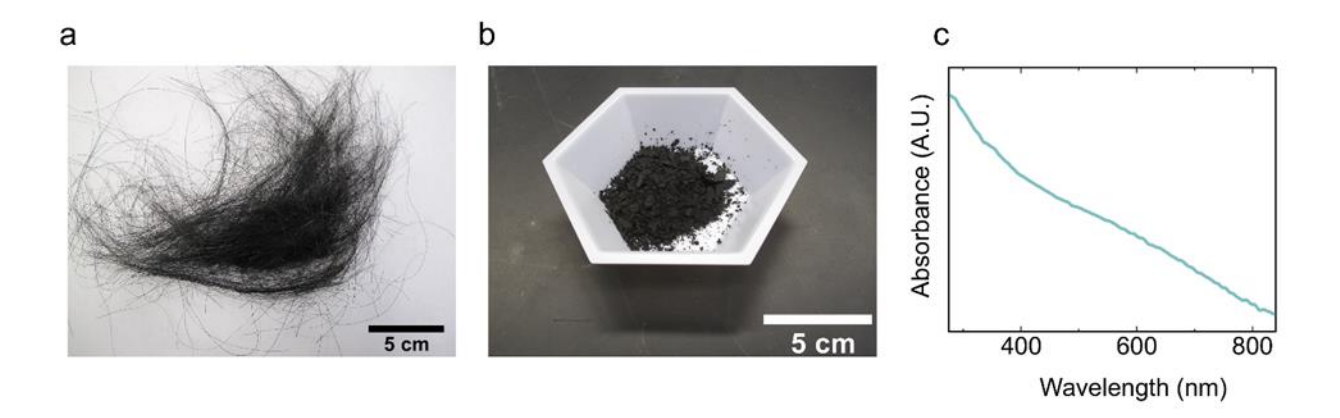


Fig. S1: (a) *Equus ferrus* hair fibers and (b) *Equus*Mel powder after extraction. (c) UV-Vis absorbance spectrum is shown for the *Equus*Mel solution (200 μ g/ml). This exhibits the broad band monotonic absorbance without the distinct peaks.

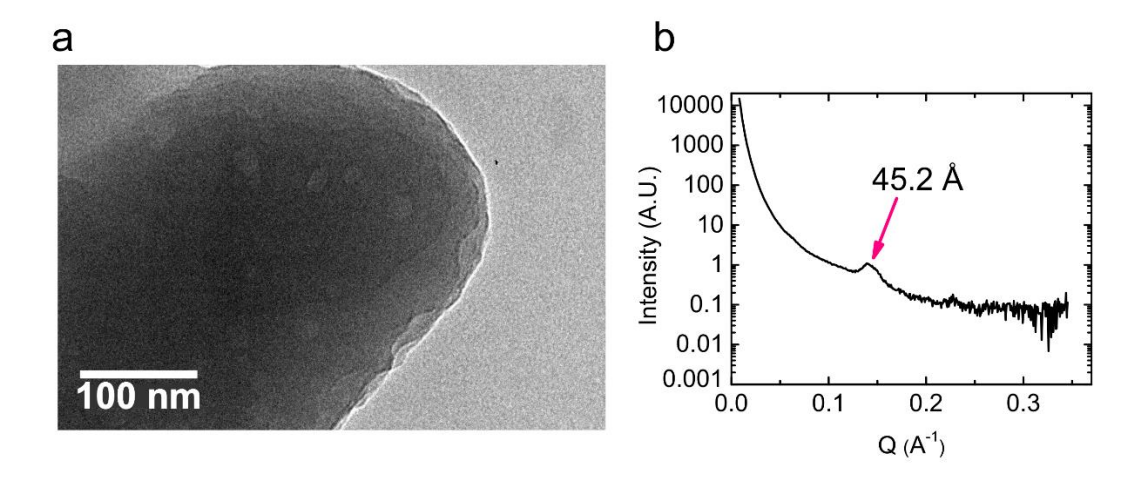


Fig. S2. Transmission electron microscopy (TEM) (a) and Small- angle X-ray scattering (SAXS) suggest that *Equus*Mel has multilayer surface with semi-crystalline structure.

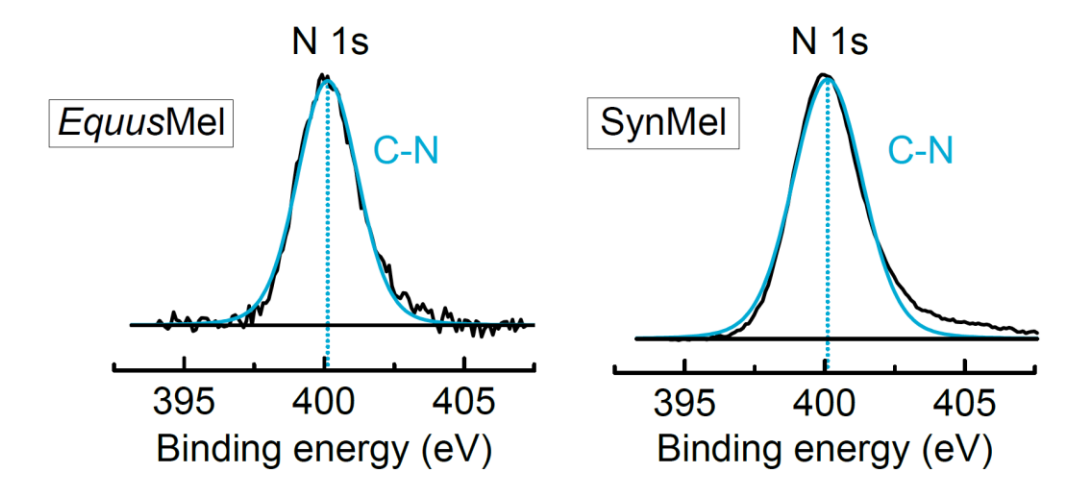


Fig. S3. High-resolution N 1s XPS spectra from *Equus*Mel and SynMel are shown. Peak fitting (blue line) is performed by CasaXPS. The peak at binding energy of 400.11 ± 0.014 represents C-N stretching from the secondary amine functional group in indole.

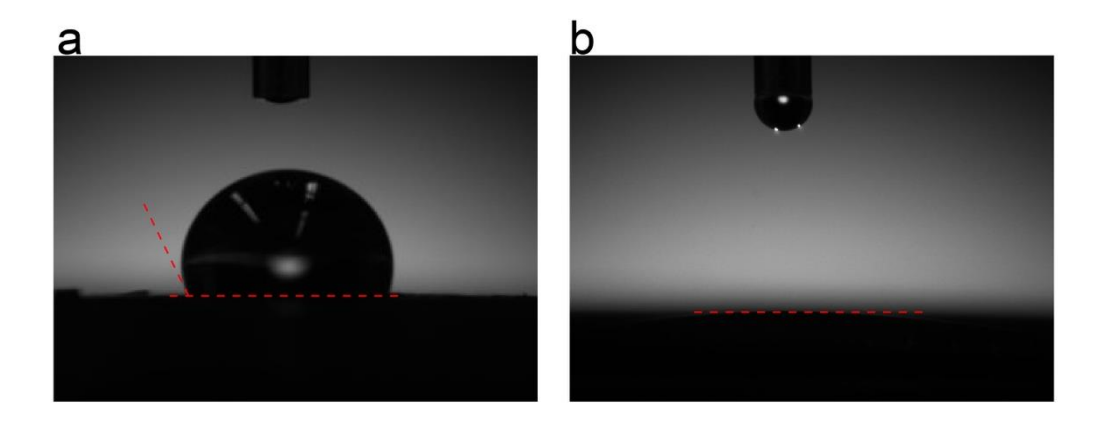


Fig. S4. Static water contact angle measurement exhibits (a) hydrophobic *Equus*Mel (contact angle= $104.7 \pm 2.2^{\circ}$) and (b) superhydrophilic SynMel (contact angle= 0°). Melanin pellets were prepared to exhibit the flat top surface before applying $10 \mu l$ of ddH_2O .

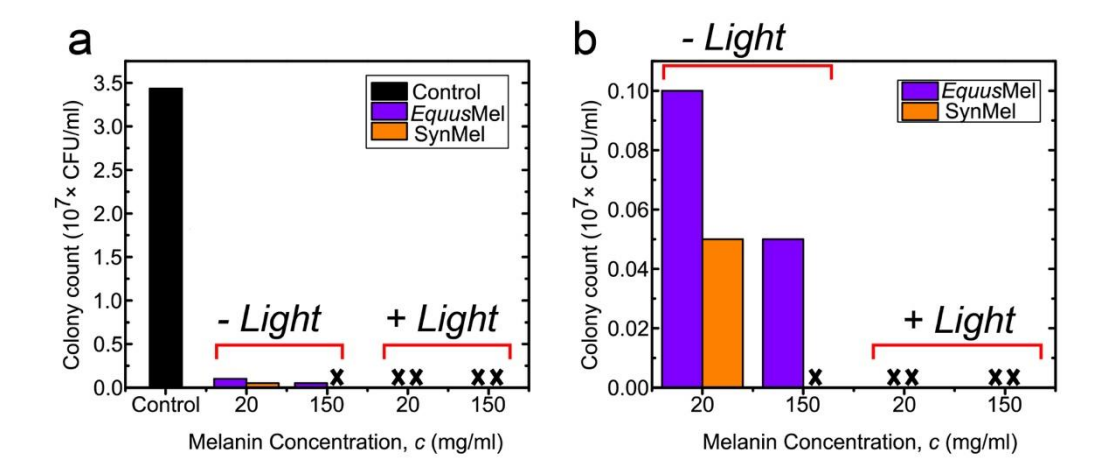


Fig. S5. (a) Antibacterial activity of *Equus*Mel and SynMel against *S. aureus* are shown after 4 h of incubation. + Light signifies that bacterial incubation with melanins occurred under ambient condition while – Light indicates light exposure was minimized as much as possible throughout the experiment from 7 days prior to incubation through colony counting. Detailed values of colony count can be found from the (b) enlarged view.

Table S1. Peak assignments of FTIR spectra for EquusMel and SynMel.

Wavenumber (cm ⁻¹)	Vibration mode and main functional groups		
3400 – 3200	Stretching vibration of O–H and N–H groups (carboxylic acid and phenolic OH, anime in indole, pyrrole, and amino acids)		
2950 - 2850	Stretching vibration of C–H		
1720 - 1706	Stretching vibration of aromatic C=O in carboxylic acid		
1650 - 1600	Stretching vibration of Conjugated C=C		
1342 – 1266	Stretching vibration of C-N in indole		
680 - 860	Bending vibration of aromatic C-H		

Table S2. Peak positions of Raman spectra of *Equus*Mel and SynMel are shown after the deconvolution using voigt function.

Peak position, cm ⁻¹			
Equus Mel	SynMel	Vibration mode and main functional groups	
1224.404	1237.68445	(α) C–O stretching in carboxylic acid and C–OH	
1348.694	1348.01362	(β) stretching vibration of aromatic C–N in indole	
1431.441	1437.68445	(γ) pyrrole ring stretching	
1507.377	1509.1941	(δ) stretching vibration of C=N in semiquinone and bending vibration of N–H	
1588.081	1575.48241	(ε) stretching vibration of aromatic C=C in indole	

Table S3. Summary of high-resolution XPS analysis of *Equus*Mel and SynMel.

Binding energy, eV							
	O 1s	N 1s	C 1s				
Equus Mel	532.17 [C-OH]	400.12 [C-N]	284.8 [C–C]/[C=C]				
	533.82 [COOH]		287.19 [C-N]/[C-O]				
SynMel	531.12 [C-O]	400.10 [C-N]	284.8 [C–C]/[C=C]				
	532.62 [C-OH]		287.26 [C-N]/[C-O]				

Table S4. Bactericidal activity of *Equus*Mel and SynMel against *E. coli* and *S. aureus* after incubating for 4 h under ambient light.

Bacterial species	E. coli		S. aureus	
Melanin Type Concentration (mg/ml)	<i>Equus</i> Mel	SynMel	<i>Equus</i> Mel	SynMel
150	100 %	100 %	100 %	100 %
20	98.12 %	100 %	100 %	100 %
5	69.06 %	98.12 %	76.67 %	98.54 %
2.5	6.87 %	61.87 %	30.1 %	93.2 %